Journal of MATERIALS RESEARCH

Article
DOI: 10.1557/jmr.2019.325

ATOMIC LAYER DEPOSITION FOR EMERGING THIN-FILM MATERIALS AND APPLICATIONS

FOCUS ISSUE

NiS_x@MoS_2 heterostructure prepared by atomic layer deposition as high-performance hydrogen evolution reaction electrocatalysts in alkaline media

Zuyun He[1], Zheng Guo[2], Qingbo Wa[2], Xiao Zhong[1,3], Xinwei Wang[2,b], Yan Chen[1,a]

[1]Guangzhou Key Laboratory for Surface Chemistry of Energy Materials, Guangdong Engineering and Technology and Research Center for Surface Chemistry of Energy Materials, State Key Laboratory of Pulp and Paper Engineering, School of Environment and Energy, South China University of Technology, Guangzhou 510006, China
[2]School of Advanced Materials, Shenzhen Graduate School, Peking University, Shenzhen 518055, China
[3]Fujian Institute of Research on the Structure of Matter, Chinese Academy of Sciences, Fuzhou 350002, China
[a)]Address all correspondence to this author. e-mail: escheny@scut.edu.cn
[b)]This author was an editor of this journal during the review and decision stage. For the JMR policy on review and publication of manuscripts authored by editors, please refer to http://www.mrs.org/editor-manuscripts/.

Received: 7 September 2019; accepted: 4 October 2019

Developing low-cost and high-performance hydrogen evolution reaction (HER) electrocatalysts is essential for the development of hydrogen energy. While transition metal sulfides are reported as promising HER electrocatalysts, their performance still requires further improvement for practical application. In this work, we report a strategy to construct NiS_x@MoS_2 heterostructures with a well-defined interface structure by growing NiS_x nanoclusters on MoS_2 nanosheets through atomic layer deposition (ALD). NiS_x@MoS_2 heterostructures exhibit strongly enhanced HER activity with lower overpotential and faster reaction dynamic compared to MoS_2 and NiS_x single phases. The enhanced performance is attributed to improved adsorption of the reaction intermediates and the facilitated charge transfer process near the MoS_2/NiS_x interfaces. Besides high activity, NiS_x@MoS_2 heterostructures also exhibit high stability in alkaline media. The methodology and knowledge in this work can guide the rational design of high-performance electrocatalysts through hetero-interface engineering.

Introduction

Hydrogen is considered to be one of the most important energy carriers due to its high energy density and environmental friendliness. Currently, most of the hydrogen are still produced from fossil fuels. Although electrochemical water splitting is believed to be a promising alternative approach for hydrogen production, its practical applications are strongly limited by the lack of cheap and highly efficient electrocatalysts for oxygen evolution reaction (OER) and hydrogen evolution reaction (HER) [1]. The mostly commonly used electrocatalysts for HER are noble metal-based materials, such as Pt/C. To lower the device prices, there have been great efforts for the synthesis of noble metal-free electrocatalysts, such as transition metal sulfides [2, 3, 4, 5], oxides [6, 7, 8, 9, 10], and carbides [11]. However, their performances still need to be further enhanced for competing with noble metal-based electrocatalysts for practical applications.

Due to its earth-abundant composition, low cost, and high activity, molybdenum disulfide (MoS_2) has been reported to be a promising candidate to substitute noble metals as high-performance HER electrocatalysts. To further improve the HER performance of MoS_2, many strategies have been investigated, such as the defects [12, 13, 14, 15] and strain engineering [16, 17], element doping [18, 19, 20, 21], morphology optimization [22, 23], and phase control [24, 25]. Recently, heterointerface engineering has emerged as an effective approach to enhance the HER activity of MoS_2 [26, 27]. For instance, Ibupoto et al. [26] reported a composite nanostructure MoS_x@NiO as an advanced nonprecious catalyst for HER in alkaline media, with an overpotential of 406 mV to produce 10 mA/cm^2 current density and the lowest Tafel slope of 43 mV per decade. Lin et al. [3] constructed defect-rich heterogeneous MoS_2/NiS_x nanosheets for overall water splitting. The interfaces of MoS_2/NiS_x with disordered structure

presented excellent electrocatalytic performance with low overpotentials of 62 mV and 278 mV at the current density of 10 mA/cm^2 for HER and OER, respectively. Yang et al. [2] designed a hierarchical nano-assemble composite $MoS_2/Co_9S_8/Ni_3S_2$/Ni with controllable composition and abundant interfaces as a highly efficient electrocatalyst for overall water splitting in a wide pH range. This hierarchical structure displays ultralow overpotentials (113, 103, and 117 mV for HER and 166, 228, and 405 mV for OER) at the current density of 10 mA/cm^2 in alkaline, acidic, and neutral electrolytes, respectively.

As mentioned above, there have been many successful examples to construct MoS_2-based heterostructures through one-step synthesis such as a solvothermal method [2, 28, 29]. However, obtaining heterostructures with a well-controlled microstructure and heterointerface properties remains a challenging task. As a consequence, the underline mechanism for the enhanced HER performance is still not well understood. It is well known that atomic layer deposition (ALD) can grow thin films with controllable thickness and composition on substrates with complex 3D structures layer by layer through alternating self-limiting surface reactions [30, 31]. Compared to other methods to construct heterointerfaces, ALD can well-maintain the microstructure of the matrix, eliminating the effect of structural changes on catalytic performances. In addition, the composition and microstructure of the heterointerface can be controlled at the atomic level, which is of great importance to obtain a fundamental understanding about the contribution of heterointerfaces to electrocatalytic activities. There have been great progresses recently in developing ALD processes for various transition metal oxides [32, 33, 34, 35, 36, 37, 38, 39, 40, 41, 42] and sulfides [30, 31, 43, 44, 45, 46, 47, 48, 49, 50]. Xiong et al. [46] designed and constructed a hybrid compound $Fe_xCo_{1-x}S_y$ electrocatalyst with controllable composition on a complex 3D structure (carbon nanotubes on carbon cloths) for HER by ALD. The best composition $Fe_{0.54}Co_{0.46}S_{0.92}$ exhibited a remarkable HER performance with a fairly low overpotential of 70 mV to achieve 10 mA/cm^2 current density in alkaline media. Li et al. [31] deposited ultrathin Co_9S_8 on carbon nanotubes by ALD for the OER, oxygen reduction reaction (ORR), and rechargeable Zn–air batteries. The ALD-prepared Co_9S_8 on carbon nanotubes presented outstanding electrocatalytic performances both for the OER and ORR with high activity and stability. Wa et al. [50] developed a new strategy to prepare an efficient electrocatalyst for electrochemical glucose sensing. ALD was used to fabricate a pre-electrocatalyst of NiS_x for $Ni(OH)_x$ with a rough surface and high electrocatalytic activity. All of these great efforts have demonstrated the capability of using the ALD technique for the rational design of high-performance energy materials.

In this work, we construct NiS_x@MoS_2 heterostructure electrocatalysts with controllable interface properties by growing NiS_x on MoS_2 nanosheets through ALD [51]. MoS_2 nanosheets were synthesized by using a hydrothermal method on carbon cloths (CCs) with a large surface area. NiS_x clusters were then deposited on the surface of MoS_2 nanosheets by ALD to build the NiS_x@MoS_2 heterostructures. The amounts of NiS_x loading on MoS_2 surface were controlled by ALD cycle numbers, ranging from 5 to 100 cycles. Scanning electron microscopy (SEM), energy-dispersive X-ray spectroscopy (EDS), X-ray photoelectron spectroscopy (XPS), and X-ray diffraction (XRD) results confirmed the formation of NiS_x@MoS_2 heterostructures. Electrochemical measurement results showed that the NiS_x@MoS_2 heterostructures exhibit an enhanced HER performance with lower overpotential and faster dynamic process due to the synergetic effects between MoS_2 and NiS_x. The NiS_x@MoS_2 nanostructures with 25 cycles of NiS_x possessed the optimal HER catalytic activity, with the overpotential of 165 mV at the current density of −10 mA/cm^2, which is 74 mV lower than that of single-phase MoS_2 nanosheets. Additionally, the NiS_x@MoS_2 heterostructure catalysts presented highly stability under operation. Our results can guild the design of high-performance electrocatalysts using ALD for other energy devices.

Results and discussion

First, the microstructure and HER activity of single-phase NiS_x grown by ALD on CCs were evaluated. Figures 1(a) and 1(b) showed the SEM images of bare CCs surface and the CCs with NiS_x grown by ALD with 100 cycles. The NiS_x was found to be nanoclusters, which distributed homogeneously on the CCs surface [Fig. 1(b)]. To verify the formation of NiS_x, EDS and XPS measurements were carried out to determine the composition of samples. As shown in Fig. 1(c), noticeable peaks of Ni and S can be observed in the EDS spectra. Figures 1(d) and 1(e) show the representative Ni 2*p* and S 2*p* XPS spectra of NiS_x on CCs. The Ni 2*p* spectrum contains two sharp peaks located at 852.7 eV and 870.0 eV, which are attributed to the spin–orbit split of $2p_{3/2}$ and $2p_{1/2}$, respectively [Fig. 1(d)]. A doublet located at 162.0 eV and 163.0 eV was ascribed to the spin–orbit split of $2p_{3/2}$ and $2p_{1/2}$ in S, respectively. The S/Ni atomic ratio of NiS_x was quantified to be ~0.8, which is consistent with our previous work [44]. The HER catalytic activity of NiS_x was examined by linear sweep voltammetry (LSV) measurement, which was performed in 1 M KOH aqueous solution using a standard three-electrode system with a slow sweep rate of 1 mV/s. Noting that all of the LSV polarization curves have been iR-corrected, where the series resistance R was determined by the current interrupt method. As shown in Fig. 1(f), the single-phase NiS_x showed poor HER catalytic activity with an overpotential of 540 mV [versus reversible hydrogen electrode (RHE)] at the current density of −10 mA/cm^2.

To construct NiS_x@MoS_2 heterostructures, MoS_2 nanosheets were first synthesized on CCs by the hydrothermal

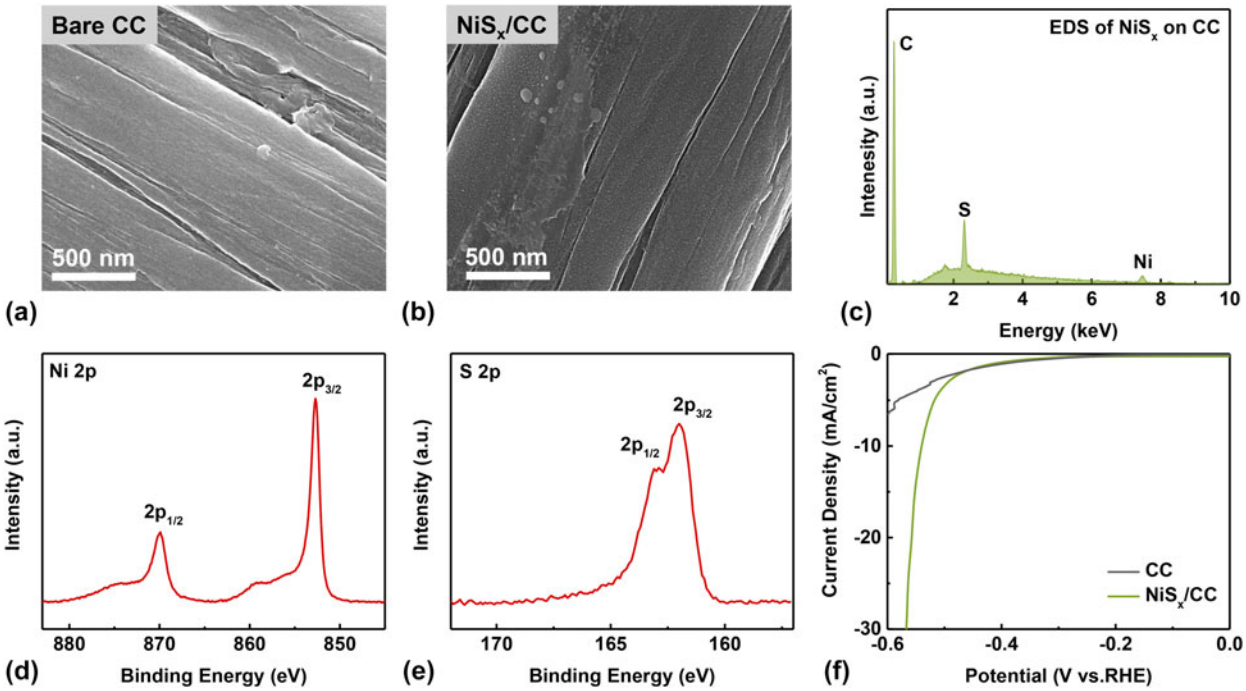

Figure 1: SEM images of (a) bare CCs, (b) NiS_x on CCs deposited by ALD with 100 cycles. (c) EDS spectrum of the NiS_x on CCs with 600 cycles (corresponding SEM image is shown in Fig. S1). (d) Ni 2*p* and (e) S 2*p* XPS spectra of NiS_x on CCs. (f) LSV curves of bare CCs and NiS_x grown by ALD with 100 cycles.

method, and NiS_x clusters were then deposited by ALD with different cycle numbers. The NiS_x@MoS_2 heterostructures with NiS_x growth cycle numbers 5, 25, and 100 are denoted as 5NiS_x@MoS_2, 25NiS_x@MoS_2, and 100NiS_x@MoS_2, respectively.

The morphology of MoS_2 nanosheets and NiS_x@MoS_2 heterostructures was probed by SEM, as shown in Fig. 2. MoS_2 nanosheets synthesized by the hydrothermal method were found to cover the CCs surface uniformly, and showed large specific surface area and abundant edges [Fig. 2(a)]. The morphology of the inset image in Fig. 2(a) shows the surface of MoS_2 nanosheets. As shown in Figs. 2(b) and 2(c), the nanosheet structure of the MoS_2 matrix can be well maintained after NiS_x deposition, while the surface of MoS_2 nanosheets become rougher with the increase in cycle number. After 100 ALD cycles, NiS_x in the form of nanoclusters were found to distribute uniformly on the surface of MoS_2 nanosheets [Fig. 2(d) inset]. The NiS_x clusters were formed because of the spontaneous agglomeration of Ni-containing species during ligand stripping in the H_2S half-cycles, and these NiS_x clusters became larger with the increase in cycle numbers [30]. NiS_x clusters anchored on the surface of MoS_2 nanosheets to construct the NiS_x@MoS_2 heterostructures and offered abundant interfaces for the HER catalysis.

The crystal structure of NiS_x@MoS_2 heterostructures was characterized by XRD and Raman measurements. As shown in Fig. 3, the XRD patterns of MoS_2 nanosheets displayed diffraction peaks at 13.7°, 32.9°, 35.6°, and 57.7°, corresponding

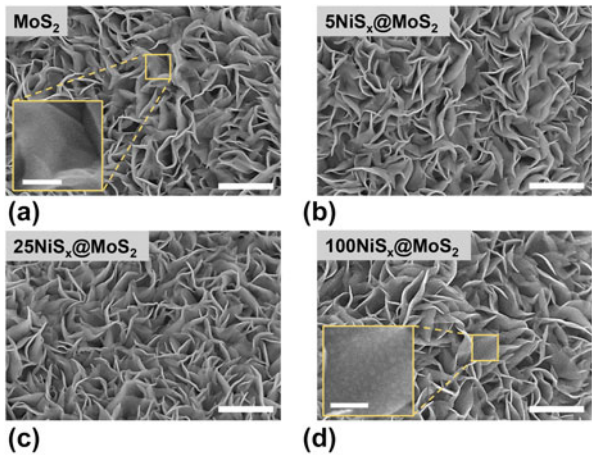

Figure 2: SEM images of (a) MoS_2 nanosheets, (b) 5NiS_x@MoS_2, (c) 25NiS_x@MoS_2, and (d) 100NiS_x@MoS_2 heterostructures with the scale bar of 500 nm. The scale bars in the inset image of a and d are 100 nm.

to the (002), (101), (103), and (110) planes of MoS_2, respectively. One possible reason for the broad diffraction peaks and the absence of high-indexed diffraction peaks is the low crystallinity and short-range disordering nature of MoS_2 grown by the hydrothermal method, which may offer a large amount of active sites for HER catalysis [52]. The small thickness of the MoS_2 flake can also contribute to the broadening of the XRD peaks. The diffraction peak located at 25.9° was attributed to

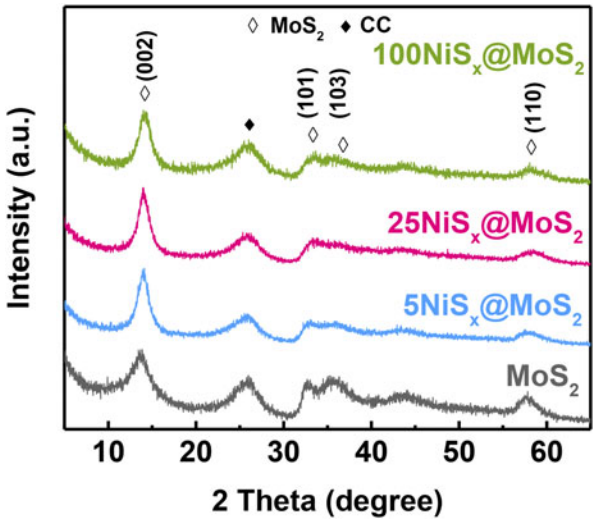

Figure 3: XRD patterns of MoS_2 nanosheets, $5NiS_x@MoS_2$, $25NiS_x@MoS_2$, and $100NiS_x@MoS_2$ heterostructures.

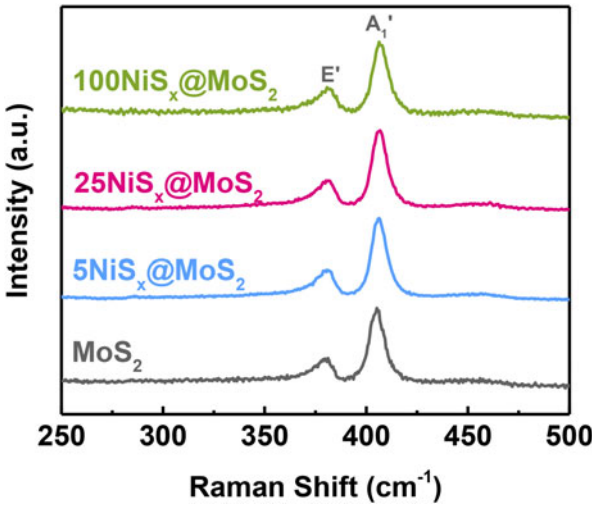

Figure 4: Raman spectra of MoS_2 nanosheets, $5NiS_x@MoS_2$, $25NiS_x@MoS_2$, and $100NiS_x@MoS_2$ heterostructures.

the carbon substrate. After ALD growth of NiS_x, the XRD patterns showed negligible changes compared to the pristine ones, which indicates that the ALD deposition of NiS_x did not change the microstructure of the MoS_2 matrix (Fig. 3). This result suggests that ALD is an ideal approach for hetero-interface engineering. Due to the small volume of NiS_x, no XRD peaks corresponding to NiS_x were observed in the XRD patterns of $NiS_x@MoS_2$ heterostructures.

The Raman spectra of MoS_2 nanosheets and $NiS_x@MoS_2$ heterostructures are shown in Fig. 4. Two Raman peaks at 405 cm^{-1} and 380 cm^{-1} can be observed, which were ascribed to the out-of-plane vibration of S atoms (A_1' peak) and the in-plane vibration of Mo and S atoms (E′ peak) in MoS_2, respectively. Note that these two Raman peaks were with a large peak width, suggesting the high disorder and defective nature of MoS_2 nanosheets, which is well consistent with the XRD results. It worth noting that no Raman peaks corresponding to NiS_x were observed in the Raman spectra of $NiS_x@MoS_2$ heterostructures due to the small volume of NiS_x.

The HER activity of MoS_2 nanosheets and $NiS_x@MoS_2$ heterostructures was systematically evaluated by electrochemical measurements. Figure 5(a) shows the LSV polarization curves for pristine MoS_2 nanosheets and $NiS_x@MoS_2$ heterostructures with 5, 25, and 100 cycles of NiS_x deposition. The pristine MoS_2 nanosheets exhibit an overpotential of 239 mV (versus. RHE) at the current density of −10 mA/cm^2. By constructing $NiS_x@MoS_2$ heterointerfaces, the HER performance had improved significantly as shown by the much lower overpotential in the LSV curves. The overpotentials at the current density of −10 mA/cm^2 were 206, 165, and 181 mV for $5NiS_x@MoS_2$, $25NiS_x@MoS_2$, and $100NiS_x@MoS_2$, respectively [Fig. 5(a)], which were 33, 74, and 58 mV lower than that for the pristine MoS_2. The HER activity of $NiS_x@MoS_2$ heterostructures first increased with the ALD cycle number of NiS_x and reached the maximum for $25NiS_x@MoS_2$. However, as the cycle number further increased to 100, the HER performance decreased.

The electrochemical impedance spectroscopy (EIS) tests, which were performed at an overpotential of 150 mV, showed consistent results as the LSV measurement. As shown in Fig. 5(b), the EIS spectra exhibit a characteristic semicircle shape, which can be fitted by an ohmic resistance, a constant phase element, and a charge transfer resistance (R_{ct}) [Fig. 5(b) inset]. The MoS_2 single-phase and $NiS_x@MoS_2$ heterostructures show similar ohmic resistance values, which are from the solution and all ohmic contacts. But the charge transfer resistance (R_{ct}), which is associated with the electrochemical reaction kinetics, is quite different between pristine MoS_2 nanosheets and $NiS_x@MoS_2$ heterostructures. The R_{ct} decreased significantly after introducing NiS_x onto the MoS_2 surface [Fig. 5(b)], which indicated a faster reaction kinetic of electrocatalysis for HER. The R_{ct} was determined to be 38.22 ohm, 10.74 ohm, 4.52 ohm, and 6.61 ohm for the pristine MoS_2 nanosheets, $5NiS_x@MoS_2$, $25NiS_x@MoS_2$, and $100NiS_x@MoS_2$, respectively. The $25NiS_x@MoS_2$ sample delivered the lowest R_{ct} value (4.52 ohm), which is about one order of magnitude lower than the R_{ct} value for pristine MoS_2 (38.22 ohm), suggesting significantly improved HER activities. Moreover, the Tafel plots were found to be 147.4 mV/dec, 122.6 mV/dec, 104.2 mV/dec, and 119.4 mV/dec for pristine MoS_2, $5NiS_x@MoS_2$, $25NiS_x@MoS_2$, and $100NiS_x@MoS_2$ heterostructures, respectively. The $25NiS_x@MoS_2$ possessed a Tafel slope (104.2 mV/decade) which was much smaller than that for MoS_2 single-phase and $NiS_x@MoS_2$ heterostructures with other compositions [Fig. 5(c)]. According to the previous works [3, 26], three

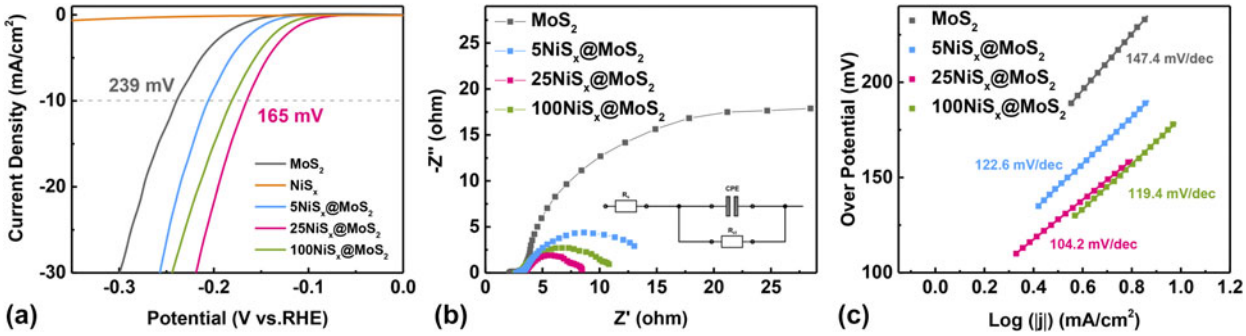

Figure 5: (a) LSV polarization curves, (b) electrochemical impedance spectroscopies, and (c) Tafel curves of MoS_2 nanosheets, $5NiS_x@MoS_2$, $25NiS_x@MoS_2$, and $100NiS_x@MoS_2$ heterostructures.

principal steps are involved in the HER process in KOH aqueous solution:

(i) Volmer step, the formation of hydrogen adsorbed intermediates (H_{ads}):

$$H_2O + e^- \rightarrow H_{ads} + OH^- \quad .$$

(ii) Heyrovsky step, the second electron transfer step:

$$H_{ads} + H_2O + e^- \rightarrow H_2 + OH^- \quad .$$

(iii) Tafel step, the combination of H_{ads}:

$$H_{ads} + H_{ads} \rightarrow H_2 \quad .$$

In general, it would be with a Tafel slope of 120, 40, or 30 mV/dec when the Volmer, Heyrovsky, or Tafel step acts as the rate-limiting and determining step for the HER, respectively [3, 26]. In this work, the Tafel slope of the MoS_2 single phase is 147.4 mV/dec, suggesting that the Volmer step is the rate-limiting step. After 25 cycles of NiS_x deposited on the MoS_2 surface, the $25NiS_x@MoS_2$ heterostructure possess a Tafel slope of 104.2 mV/dec, which indicated that the rate-limiting step changes to the Volmer–Heyrovsky step, suggesting a facilitated electron transfer and improved adsorption for the reacting intermediates due to the formation of rich interfaces. It has been reported that the binding free energy of H_{ads} intermediates is −0.33 eV for the pristine MoS_2 catalyst sites, which is favorable to the hydrogen generation step (Heyrovsky step or Tafel step). However, the MoS_2 exhibits a high barrier of 1.17 eV for H–OH adsorption, which hinders the dissociation of H_2O to form H_{ads} intermediates (Volmer step), resulting in the sluggish hydrogen evolution kinetics [53]. Zhang et al. [29] suggested that the presence of $NiS_x@MoS_2$ interfaces could facilitate the chemisorption of hydrogen and oxygen-containing intermediates, which can promote the initial water dissociation step (Volmer step). Furthermore, density functional theory (DFT) calculation [29] also showed that the chemisorption free energies of hydrogen and hydroxide on the interfaces were lower than that on the surface of MoS_2 and NiS_x single phases. As a result, the interfaces between MoS_2 and NiS_x show a synergistic effect that MoS_2 exhibits a favorable free energy for H_{ads} intermediates and NiS_x can promote the adsorption of oxygen-containing intermediates, which may accelerate the HER processes, resulting in the enhanced electrocatalytic performance.

All the electrochemical measurement results consistently suggest that the HER catalytic activity of $NiS_x@MoS_2$ heterostructures is significantly higher than that of MoS_2 single-phase nanosheets. Since pure NiS_x grown by ALD showed negligible contribution to the HER activity [Figs. 1(d) and 5(a)], the enhanced HER activity of $NiS_x@MoS_2$ was likely due to the presence of NiS_x/MoS_2 heterointerfaces. As shown in the electrochemical test results and in previous literatures [3, 29], the presence of NiS_x/MoS_2 heterointerfaces can provide rich electrocatalytic active sites, enhancing the adsorption of reaction intermediates, improving electronic conductivity, and facilitating the electron transfer process. It is important to note that the HER performance of $NiS_x@MoS_2$ heterostructures first improved with the NiS_x cycle number, but reached the maximum for the cycle number of 25. As discussed above, the area near the NiS_x, MoS_2, and electrolyte triple-phase boundary is believed to be the activity region of the HER. As the ALD cycle number increased, such active regions first increased because of more NiS_x and MoS_2 interfacial regions being exposed to the electrolytes, leading to improved activity. Further increase in NiS_x coverage resulted in the decrease of the triple-phase boundary region, which led to the degradation of HER activity as observed above for $100NiS_x@MoS_2$.

Operational stability is another critical factor that should be taken into account in practical applications. Thereby, the long-term stability of $NiS_x@MoS_2$ heterostructures was also evaluated. The chronopotentiometry measurement (CP) was performed at the current density of -10 mA/cm^2 for 20 h in 1 M KOH. The overpotential at the current density of -10 mA/cm^2 of MoS_2 and

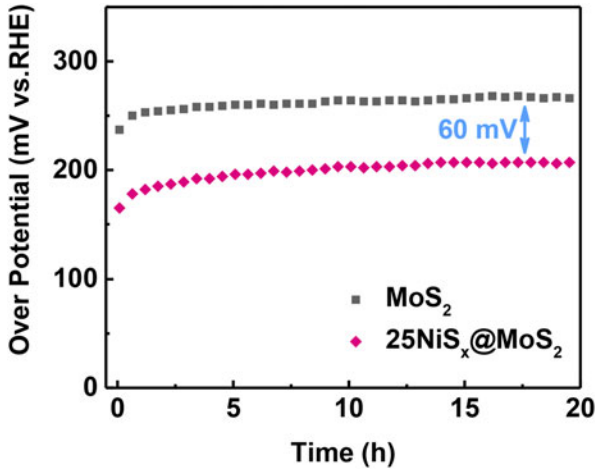

Figure 6: Chronopotentiometry curves at the current density of −10 mA/cm^2 of MoS_2 nanosheets and 25NiS_x@MoS_2 heterostructure.

25NiS_x@MoS_2 samples was compared over time. As shown in Fig. 6, both MoS_2 and 25NiS_x@MoS_2 remain stable during operation, indicating a firm combination of MoS_2 and NiS_x and a negligible exfoliation of NiS_x clusters over operation. The overpotential of 25NiS_x@MoS_2 is still 60 mV lower than that of pristine MoS_2, suggesting good long-term stability and excellent HER performance.

Conclusion

In summary, we developed a novel strategy to construct NiS_x@MoS_2 heterostructures controllably through the combination of a hydrothermal method and ALD techniques. MoS_2 nanosheets with a large surface area and abundant edge sites were synthesized on CCs substrates. After ALD deposition, homogeneous NiS_x clusters were anchored on the surface of MoS_2 nanosheets. SEM and XRD results confirmed that the morphology and structure of MoS_2 can be well maintained during the ALD process. NiS_x@MoS_2 heterostructures exhibited a strongly enhanced HER performance with lower overpotential and faster dynamic process compared with single-phase MoS_2 nanosheets. The NiS_x@MoS_2 heterostructures with 25 ALD cycles of NiS_x deposition showed the optimal HER catalytic activity, with a decreased overpotential of 74 mV at the current density of −10 mA/cm^2 than the pristine MoS_2 nanosheets. Additionally, the NiS_x@MoS_2 heterostructure catalysts present highly stability under operation in alkaline media. The high electrocatalytic activity of NiS_x@MoS_2 for HER was attributed to the presence of NiS_x/MoS_2 heterointerfaces, which not only provide high-density electrocatalytic active sites for the adsorption of reaction intermediates but also promote the electron transfer process. While NiS_x@MoS_2 was taken as the model system in this work, the methodology and knowledge can also apply to construct other transition metal oxide or sulfide heterostructure electrocatalysts for various reactions, such as OER, ORR, and CO_2 reduction reaction.

Experimental section

Synthesis of MoS_2 nanosheets and NiS_x@MoS_2 heterostructures

MoS_2 nanosheets were synthesized by a hydrothermal method. Ammonium molybdate tetrahydrate [$(NH_4)_6Mo_7O_{24}{\cdot}4H_2O$] and thiourea ($CH_4N_2S$) were dissolved in water and sonicated for 30 min to form a homogeneous and pellucid solution, which was then transferred into a Teflon-lined stainless-steel autoclave for MoS_2 synthesis. The pH of the solution was adjusted to 3. The autoclave was heated to 180 °C for 24 h and then allowed to cool to room temperature naturally. CCs was used as the substrate for growing the MoS_2 nanosheets. The resulting samples were washed with ultra-pure water several times to remove the excess reactant and then dried at 60 °C overnight. The NiS_x was grown on MoS_2 nanosheets by ALD at 120 °C using bis(*N*,*N*′-*di*-*tert*-butylacetamidinato)nickel(II) ($Ni(amd)_2$) and H_2S as precursors in a home-built tubular reactor. Details of the NiS_x ALD process are reported in our previous works [30, 44, 49]. The amount of NiS_x deposited on MoS_2 was controlled by the number of ALD cycles, ranging from 5 to 100 cycles.

Characterization

The morphologies of NiS_x@MoS_2 heterostructures, and NiS_x and MoS_2 single-phase reference samples were characterized by high-resolution field emission SEM (SU8010, Hitachi, Tokyo, Japan). Electron energy of 5 kV was used for morphology characterization. EDS was carried out to determine the chemical composition of the materials. The crystal structures of the materials were characterized by XRD using Bruker D8 Advance (Karlsruhe, Germany) with monochromatized Cu K_α radiation. The Raman spectra were measured by a confocal microscopic system (LabRAM HR Evolution, Horiba, Pairs, France) equipped with a green laser (λ = 532 nm, Laser Quantum Ltd., Stockport, U.K.), and a 100× objective lens was used to focus the laser to a spot with size of 1 μm.

Electrochemical measurements

The HER performance of samples was measured by a CHI 660E electrochemical workstation (CH Instruments, Shanghai, China) using a standard three-electrode system in 1 M KOH aqueous solution. The NiS_x@MoS_2 heterostructures, and MoS_2 and NiS_x single-phase reference samples on CCs served as the working electrode, and a carbon rod was used as the counter electrode. A Ag/AgCl electrode prefilled with saturated KCl aqueous solution was used as the reference electrode. LSV

measurements were carried out at 1 mV/s. EIS was measured at 150 mV versus RHE with an amplitude of 5 mV and a frequency range from 10^6 to 10^{-2} Hz. Chronopotentiometry tests were carried out at a constant current density of −10 mA/cm^2 for 20 h.

Acknowledgment

This work was supported by the National Natural Science Foundation of China (11605063, 51672011, and 11975102), Guangzhou Science and Technology Program General Projects (201707010146), the Fundamental Research Funds for the Central Universities (2018MS40), State Key Laboratory of Pulp and Paper Engineering (2018TS08), Guangdong Pearl River Talent Program (2017GC010281), and Guangdong Innovative and Entrepreneurial Research Team Program (2014ZT05N200) and Natural Science Foundation of Fujian Province (No. 2015J01068).

Supplementary material

To view supplementary material for this article, please visit https://doi.org/10.1557/jmr.2019.325.

References

1. **S. Anantharaj, S.R. Ede, K. Sakthikumar, K. Karthick, S. Mishra, and S. Kundu**: Recent trends and perspectives in electrochemical water splitting with an emphasis on sulfide, selenide, and phosphide catalysts of Fe, Co, and Ni: A review. *ACS Catal.* **6**, 8069–8097 (2016).
2. **Y. Yang, H. Yao, Z. Yu, S.M. Islam, H. He, M. Yuan, Y. Yue, K. Xu, W. Hao, G. Sun, H. Li, S. Ma, P. Zapol, and M.G. Kanatzidis**: Hierarchical nanoassembly of $MoS_2/Co_9S_8/Ni_3S_2$/Ni as a highly efficient electrocatalyst for overall water splitting in a wide pH range. *J. Am. Chem. Soc.* **141**, 10417–10430 (2019).
3. **J. Lin, P. Wang, H. Wang, C. Li, X. Si, J. Qi, J. Cao, Z. Zhong, W. Fei, and J. Feng**: Defect-rich heterogeneous MoS_2/NiS_2 nanosheets electrocatalysts for efficient overall water splitting. *Adv. Sci.* **6**, 1900246 (2019).
4. **Q. Zhang, W. Wang, J. Zhang, X. Zhu, Q. Zhang, Y. Zhang, Z. Ren, S. Song, J. Wang, Z. Ying, R. Wang, X. Qiu, T. Peng, and L. Fu**: Highly efficient photocatalytic hydrogen evolution by ReS_2 via a two-electron catalytic reaction. *Adv. Mater.* **30**, e1707123 (2018).
5. **Y. Wu, X. Liu, D. Han, X. Song, L. Shi, Y. Song, S. Niu, Y. Xie, J. Cai, S. Wu, J. Kang, J. Zhou, Z. Chen, X. Zheng, X. Xiao, and G. Wang**: Electron density modulation of $NiCo_2S_4$ nanowires by nitrogen incorporation for highly efficient hydrogen evolution catalysis. *Nat. Commun.* **9**, 1425 (2018).
6. **Z. Xiao, Y. Wang, Y-C. Huang, Z. Wei, C-L. Dong, J. Ma, S. Shen, Y. Li, and S. Wang**: Filling the oxygen vacancies in Co_3O_4 with phosphorus: An ultra-efficient electrocatalyst for overall water splitting. *Energy Environ. Sci.* **10**, 2563–2569 (2017).
7. **H. Jin, J. Wang, D. Su, Z. Wei, Z. Pang, and Y. Wang**: In situ cobalt–cobalt oxide/N-doped carbon hybrids as superior bifunctional electrocatalysts for hydrogen and oxygen evolution. *J. Am. Chem. Soc.* **137**, 2688–2694 (2015).
8. **Y. Zhu, X. Liu, S. Jin, H. Chen, W. Lee, M. Liu, and Y. Chen**: Anionic defect engineering of transition metal Xxides for oxygen reduction and evolution reactions. *J. Mater. Chem. A* **7**, 5875–5897 (2019).
9. **Y. Zhu, L. Zhang, B. Zhao, H. Chen, X. Liu, R. Zhao, X. Wang, J. Liu, Y. Chen, and M. Liu**: Improving the activity for oxygen evolution reaction by tailoring oxygen defects in double perovskite oxides. *Adv. Funct. Mater.* **29**, 1901783 (2019).
10. **X. Liu, L. Zhang, Y. Zheng, Z. Guo, Y. Zhu, H. Chen, F. Li, P. Liu, B. Yu, X. Wang, J. Liu, Y. Chen, and M. Liu**: Uncovering the effect of lattice strain and oxygen deficiency on electrocatalytic activity of perovskite cobaltite thin films. *Adv. Sci.* **6**, 1801898 (2019).
11. **Y. Zang, S. Niu, Y. Wu, X. Zheng, J. Cai, J. Ye, Y. Xie, Y. Liu, J. Zhou, J. Zhu, X. Liu, G. Wang, and Y. Qian**: Tuning orbital orientation endows molybdenum disulfide with exceptional alkaline hydrogen evolution capability. *Nat. Commun.* **10**, 1217 (2019).
12. **Y. Chen, S. Huang, X. Ji, K. Adepalli, K. Yin, X. Ling, X. Wang, J. Xue, M. Dresselhaus, J. Kong, and B. Yildiz**: Tuning electronic structure of single layer MoS_2 through defect and interface engineering. *ACS Nano* **12**, 2569–2579 (2018).
13. **Z. He, R. Zhao, X. Chen, H. Chen, Y. Zhu, H. Su, S. Huang, J. Xue, J. Dai, S. Cheng, M. Liu, X. Wang, and Y. Chen**: Defect engineering in single-layer MoS_2 using heavy ion irradiation. *ACS Appl. Mater. Interfaces* **10**, 42524–42533 (2018).
14. **L. Li, Z. Qin, L. Ries, S. Hong, T. Michel, J. Yang, C. Salameh, M. Bechelany, P. Miele, D. Kaplan, M. Chhowalla, and D. Voiry**: Role of sulfur vacancies and undercoordinated Mo regions in MoS_2 nanosheets toward the evolution of hydrogen. *ACS Nano* **13**, 6824–6834 (2019).
15. **C. Tsai, H. Li, S. Park, J. Park, H.S. Han, J.K. Norskov, X. Zheng, and F. Abild-Pedersen**: Electrochemical generation of sulfur vacancies in the basal plane of MoS_2 for hydrogen evolution. *Nat. Commun.* **8**, 15113 (2017).
16. **H. Li, C. Tsai, A.L. Koh, L. Cai, A.W. Contryman, A.H. Fragapane, J. Zhao, H.S. Han, H.C. Manoharan, F. Abild-Pedersen, J.K. Norskov, and X. Zheng**: Activating and optimizing MoS_2 basal planes for hydrogen evolution through the formation of strained sulphur vacancies. *Nat. Mater.* **15**, 364 (2016).
17. **H. Li, M. Du, M.J. Mleczko, A.L. Koh, Y. Nishi, E. Pop, A.J. Bard, and X. Zheng**: Kinetic study of hydrogen evolution reaction over strained MoS_2 with sulfur vacancies using scanning

electrochemical microscopy. *J. Am. Chem. Soc.* **138**, 5123–5129 (2016).

18. **W. Xiao, P. Liu, J. Zhang, W. Song, Y.P. Feng, D. Gao, and J. Ding**: Dual-functional N dopants in edges and basal plane of MoS_2 nanosheets toward efficient and durable hydrogen evolution. *Adv. Energy Mater.* **7**, 1602086 (2017).
19. **P. Liu, J. Zhu, J. Zhang, P. Xi, K. Tao, D. Gao, and D. Xue**: P dopants triggered new basal plane active sites and enlarged interlayer spacing in MoS_2 nanosheets toward electrocatalytic hydrogen evolution. *ACS Energy Lett.* **2**, 745–752 (2017).
20. **Z. Luo, Y. Ouyang, H. Zhang, M. Xiao, J. Ge, Z. Jiang, J. Wang, D. Tang, X. Cao, C. Liu, and W. Xing**: Chemically activating MoS_2 via spontaneous atomic palladium interfacial doping towards efficient hydrogen evolution. *Nat. Commun.* **9**, 2120 (2018).
21. **T. Sun, J. Wang, X. Chi, Y. Lin, Z. Chen, X. Ling, C. Qiu, Y. Xu, L. Song, W. Chen, and C. Su**: Engineering the electronic structure of MoS_2 nanorods by N and Mn dopants for ultra-efficient hydrogen production. *ACS Catal.* **8**, 7585–7592 (2018).
22. **D. Kong, H. Wang, J.J. Cha, M. Pasta, K.J. Koski, J. Yao, and Y. Cui**: Synthesis of MoS_2 and $MoSe_2$ films with vertically aligned layers. *Nano Lett.* **13**, 1341–1347 (2013).
23. **J. Kibsgaard, Z. Chen, B.N. Reinecke, and T.F. Jaramillo**: Engineering the surface structure of MoS_2 to preferentially expose active edge sites for electrocatalysis. *Nat. Mater.* **11**, 963–969 (2012).
24. **S. Wang, D. Zhang, B. Li, C. Zhang, Z. Du, H. Yin, X. Bi, and S. Yang**: Ultrastable in-plane 1T-2H MoS_2 heterostructures for enhanced hydrogen evolution reaction. *Adv. Energy Mater.* **8**, 1801345 (2018).
25. **Y. Yin, J. Han, Y. Zhang, X. Zhang, P. Xu, Q. Yuan, L. Samad, X. Wang, Y. Wang, Z. Zhang, P. Zhang, X. Cao, B. Song, and S. Jin**: Contributions of phase, sulfur vacancies, and edges to the hydrogen evolution reaction catalytic activity of porous molybdenum disulfide nanosheets. *J. Am. Chem. Soc.* **138**, 7965–7972 (2016).
26. **Z.H. Ibupoto, A. Tahira, P. Tang, X. Liu, J.R. Morante, M. Fahlman, J. Arbiol, M. Vagin, and A. Vomiero**: MoS_x@nio composite nanostructures: An advanced nonprecious catalyst for hydrogen evolution reaction in alkaline media. *Adv. Funct. Mater.* **29**, 1807562 (2019).
27. **A. Khalil, Q. Liu, Z. Muhammad, M. Habib, R. Khan, Q. He, Q. Fang, H.T. Masood, Z.U. Rehman, T. Xiang, C.Q. Wu, and L. Song**: Synthesis of Ni_9S_8/MoS_2 heterocatalyst for enhanced hydrogen evolution reaction. *Langmuir* **33**, 5148–5153 (2017).
28. **S. Li, T. Chen, J. Wen, P. Gui, and G. Fang**: In situ grown Ni_9S_8 nanorod/O-MoS_2 nanosheet nanocomposite on carbon cloth as a free binder supercapacitor electrode and hydrogen evolution catalyst. *Nanotechnology* **28**, 445407 (2017).
29. **J. Zhang, T. Wang, D. Pohl, B. Rellinghaus, R. Dong, S. Liu, X. Zhuang, and X. Feng**: Interface engineering of MoS_2/Ni_3S_2 heterostructures for highly enhanced electrochemical overall-water-splitting activity. *Angew. Chem., Int. Ed. Engl.* **55**, 6702–6707 (2016).
30. **R. Zhao and X. Wang**: Initial growth and agglomeration during atomic layer deposition of nickel sulfide. *Chem. Mater.* **31**, 445–453 (2019).
31. **H. Li, Z. Guo, and X. Wang**: Atomic-layer-deposited ultrathin Co_9S_8 on carbon nanotubes: an efficient bifunctional electrocatalyst for oxygen evolution/reduction reactions and rechargeable Zn–air batteries. *J. Mater. Chem. A* **5**, 21353–21361 (2017).
32. **X. Wang, O.I. Saadat, B. Xi, X. Lou, R.J. Molnar, T. Palacios, and R.G. Gordon**: Atomic layer deposition of Sc_2O_3 for passivating AlGaN/GaN high electron mobility transistor devices. *Appl. Phys. Lett.* **101**, 232109 (2012).
33. **X. Wang, L. Dong, J. Zhang, Y. Liu, P.D. Ye, and R.G. Gordon**: Heteroepitaxy of La_2O_3 and $La_{(2-x)}Y_{(x)}O_3$ on GaAs(111)A by atomiclayer deposition: Achieving low interface trap density. *Nano Lett.* **13**, 594–599 (2013).
34. **Q. Sheng, L. Wang, C. Wang, X. Wang, and J. Xue**: Fabrication of nanofluidic diodes with polymer nanopores modified by atomic layer deposition. *Biomicrofluidics* **8**, 052111 (2014).
35. **Y. Su, S. Cui, Z. Zhuo, W. Yang, X. Wang, and F. Pan**: Enhancing the high-voltage cycling performance of $LiNi_{(0.5)}Mn_{(0.3)}Co_{(0.2)}O_2$ by retarding its interfacial reaction with an electrolyte by atomic-layer-deposited Al_2O_3. *ACS Appl. Mater. Interfaces* **7**, 25105–25112 (2015).
36. **C. Wang, Q. Fu, X. Wang, D. Kong, Q. Sheng, Y. Wang, Q. Chen, and J. Xue**: Atomic layer deposition modified track-etched conical nanochannels for protein sensing. *Anal. Chem.* **87**, 8227–8233 (2015).
37. **Y. Gao, Y. Shao, L. Yan, H. Li, Y. Su, H. Meng, and X. Wang**: Efficient charge injection in organic field-effect transistors enabled by low-temperature atomic layer deposition of ultrathin VO_x interlayer. *Adv. Funct. Mater.* **26**, 4456–4463 (2016).
38. **X. Lou, H. Zhou, S.B. Kim, S. Alghamdi, X. Gong, J. Feng, X. Wang, P.D. Ye, and R.G. Gordon**: Epitaxial growth of $Mg_xCa_{1-x}O$ on GaN by atomic layer deposition. *Nano Lett.* **16**, 7650–7654 (2016).
39. **Y. Su, C. Xin, Y. Feng, Q. Lin, X. Wang, J. Liang, J. Zheng, Y. Lin, and F. Pan**: Band alignment for rectification and tunneling effects in Al_2O_3 atomic-layer-deposited on back contact for CdTe solar cell. *ACS Appl. Mater. Interfaces* **8**, 28143–28148 (2016).
40. **X. Wang, Z. Guo, Y. Gao, and J. Wang**: Atomic layer deposition of vanadium oxide thin films from tetrakis(dimethylamino) vanadium precursor. *J. Mater. Res.* **32**, 37–44 (2016).
41. **R. Zhao, Y. Gao, Z. Guo, Y. Su, and X. Wang**: Interface energy alignment of atomic-layer-deposited VO_x on pentacene: An in situ photoelectron spectroscopy investigation. *ACS Appl. Mater. Interfaces* **9**, 1885–1890 (2017).
42. **Y. Gao, Y. Shi, H. Meng, and X. Wang**: Onset voltage shift in the organic thin-film transistor with an atomic-layer-deposited charge-injection interlayer. *Org. Electron.* **62**, 248–252 (2018).

43. **H. Li, Y. Gao, Y. Shao, Y. Su, and X. Wang**: Vapor-phase atomic layer deposition of Co_9S_8 and its application for supercapacitors. *Nano Lett.* **15**, 6689–6695 (2015).
44. **H. Li, Y. Shao, Y. Su, Y. Gao, and X. Wang**: Vapor-phase atomic layer deposition of nickel sulfide and its application for efficient oxygen-evolution electrocatalysis. *Chem. Mater.* **28**, 1155–1164 (2016).
45. **Y. Shao, Z. Guo, H. Li, Y. Su, and X. Wang**: Atomic layer deposition of iron sulfide and its application as a catalyst in the hydrogenation of azobenzenes. *Angew Chem. Int. Ed. Engl.* **56**, 3226–3231 (2017).
46. **W. Xiong, Z. Guo, H. Li, R. Zhao, and X. Wang**: Rational bottom-up engineering of electrocatalysts by atomic layer deposition: A case study of $Fe_xCo_{1-x}S_y$-based catalysts for electrochemical hydrogen evolution. *ACS Energy Lett* **2**, 2778–2785 (2017).
47. **Z. Guo and X. Wang**: Atomic layer deposition of the metal pyrites FeS_2, CoS_2, and NiS_2. *Angew. Chem., Int. Ed. Engl.* **57**, 5898–5902 (2018).
48. **J. Wang, Z. Guo, W. Xiong, and X. Wang**: Synthesis of thin-film metal pyrites by an atomic layer deposition approach. *Chemistry* **24**, 18568–18574 (2018).
49. **R. Zhao, Z. Guo, and X. Wang**: Surface chemistry during atomic-layer deposition of nickel sulfide from nickel amidinate and H_2S. *J. Phys. Chem. C* **122**, 21514–21520 (2018).
50. **Q. Wa, W. Xiong, R. Zhao, Z. He, Y. Chen, and X. Wang**: Nanoscale $Ni(OH)_x$ films on carbon cloth prepared by atomic layer deposition and electrochemical activation for glucose sensing. *ACS Appl. Nano Mater* **2**, 4427–4434 (2019).
51. **X. Meng, X. Wang, D. Geng, C. Ozgit-Akgun, N. Schneider, and J.W. Elam**: Atomic layer deposition for nanomaterial synthesis and functionalization in energy technology. *Mater. Horiz.* **4**, 133–154 (2017).
52. **J. Xie, J. Zhang, S. Li, F. Grote, X. Zhang, H. Zhang, R. Wang, Y. Lei, B. Pan, and Y. Xie**: Controllable disorder engineering in oxygen-incorporated MoS_2 ultrathin nanosheets for efficient hydrogen evolution. *J. Am. Chem. Soc.* **135**, 17881–17888 (2013).
53. **B. Zhang, J. Liu, J. Wang, Y. Ruan, X. Ji, K. Xu, C. Chen, H. Wan, L. Miao, and J. Jiang**: Interface engineering: The $Ni(OH)_2$/MoS_2 heterostructure for highly efficient alkaline hydrogen evolution. *Nano Energy* **37**, 74–80 (2017).